INT. J. REMOTE SENSING, 20 NOVEMBER, 2003,
VOL. 24, NO. 22, 4505–4525

Taylor & Francis
Taylor & Francis Group

A multi-year active fire dataset for the tropics derived from the TRMM VIRS

L. GIGLIO*, J. D. KENDALL

Science Systems and Applications, Inc., NASA Goddard Space Flight Center, Code 923, Greenbelt, MD 20771, USA

and R. MACK

NASA Goddard Space Flight Center, Code 902, Greenbelt, MD 20771, USA

(*Received 3 July 2001; in final form 10 September 2002*)

Abstract. A pan-tropical active fire dataset derived from observations made with the Visible and Infrared Scanner (VIRS), onboard the Tropical Rainfall Measuring Mission (TRMM) satellite, is described. The dataset consists of monthly 0.5° resolution fire summary products from January 1998 to the present, with geographical coverage spanning latitudes 38° S to 38° N. Several key issues previously not considered in summarizing satellite-derived fire 'counts' were addressed during development of the product. The dataset is intended to provide a current, continuous, multi-year record of fire activity in the tropics and subtropics for input to global studies on the Earth's land and atmosphere processes, their interaction, and relation to climate change. Following the availability of improved global fire coverage from the Moderate Resolution Imaging Spectroradiometer (MODIS), the VIRS fire dataset will continue to be useful because it can provide new multi-year information on the diurnal cycle of fire that is difficult to achieve at the global scale. Development of an efficient, operational production stream for this dataset was achieved through an innovative and cost-effective data-mining activity at the Goddard Earth Sciences Distributed Active Archive Center (GES DAAC). For the remainder of the expected six-year lifespan of the TRMM spacecraft (through 2003), the VIRS fire products will continue to be generated through cooperation with the GES DAAC. Facilities for Web-based distribution of the products are currently being developed at http://daac.gsfc.nasa.gov.

1. Introduction

Since reliable ground-based estimates of vegetation fire activity are available only for the industrial countries of the Northern Hemisphere and a few limited regions in the Southern Hemisphere, satellite remote sensing plays an important role in the development of biomass burning datasets which are required for regional and global studies on: land use/land cover change, carbon and trace gas emissions

*Corresponding author; e-mail: giglio@hades.gsfc.nasa.gov

International Journal of Remote Sensing
ISSN 0143-1161 print/ISSN 1366-5901 online © 2003 Taylor & Francis Ltd
http://www.tandf.co.uk/journals
DOI: 10.1080/0143116031000070283

to the atmosphere, and their implications for climate change (Justice and Korontzi 2000).

During the past decade, a number of regional and/or continental scale fire datasets have been assembled using measurements from coarse resolution meteorological satellite sensors including: the Geostationary Orbiting Environmental Satellite (GOES) Imager, the Operational Linescan System (OLS), the Along Track Scanning Radiometer (ATSR) and the Advanced Very High Resolution Radiometer (AVHRR) (Giglio *et al.* 2000). To date, such products have provided a rough baseline of fire distribution worldwide and some qualitative information for parametrizing input on biomass burning emissions for global models. However, due to several limitations, the existing datasets have not been able to improve substantially the major uncertainties in estimates of fire activity and emissions from biomass burning (Kaufman *et al.* 1998).

One of the key limitations is scarcity of appropriate satellite fire products. Continuous global coverage has only been achieved for two periods spanning more than a year: an 18-month period in 1992–1993 using daytime National Oceanic and Atmospheric Administration (NOAA) AVHRR data and a three-year period (August 1996–July 1999) using night-time ATSR data (Stroppiana *et al.* 2000, Arino *et al.* 2001). While there is a reasonable amount of recent regional and/or continental fire products, their temporal and diurnal coverage varies substantially rendering comparison of data quality and retrievable information content extremely difficult. In addition, none of the existing products has explicitly addressed bias issues related to summarizing pixel counts in multitemporal products. This creates another complication for efforts to ascertain the quality of fire information extracted.

The launch of the EOS-AM1 (or Terra) platform in late 1999 marked the beginning of a new era in satellite fire detection. Terra's Moderate Resolution Imaging Spectroradiometer (MODIS) instrument has 1 km resolution mid- and long-wave infrared channels designed specifically for observing active fires. With MODIS observations, for the first time, a continuous multi-year global fire dataset will ultimately be available to provide improved information on global vegetation fire activity (Justice *et al.* 1998). While MODIS observations will significantly improve current capabilities for remote sensing of fire activity, the existence of a multi-year dataset from MODIS will not be achieved for several more years. Due to initial post-launch instrument problems, the start date for the archive of usable, long-term active fire products did not begin until November 2000. In addition, forthcoming results indicate that the late morning local overpass time of the Terra spacecraft (10:30) may be suboptimal for observation of wildfires in certain regions. For these areas, observations from the EOS-PM1 (or Aqua) platform, with its early afternoon (13:30) overpass, will provide superior data. A continuous archive of global fire data from Aqua MODIS is expected to begin in early 2002.

Although intended for cross-calibrating precipitation measurements derived from the Tropical Rainfall Measuring Mission (TRMM) Microwave Imager and Precipitation Radar instruments with those derived from the heritage geostationary satellite systems [e.g. Geostationary Meteorological Satellite (GMS), GOES], the Visible and Infrared Scanner (VIRS) carries mid- and long-wave infrared channels that also make it useful for observing active fires. Since the tropical and subtropical regions that fall within TRMM's observational path present some of our greatest

uncertainties in estimates of biomass burning emissions, VIRS offers an excellent opportunity for generating a new multi-year fire dataset. This may prove especially useful for filling critical data gaps in Earth science and climate change research during the period prior to the availability of multi-year global fire observations from MODIS.

In this paper we describe the preparation and preliminary evaluation of a pan-tropical active fire dataset derived from the current VIRS archive, spanning January 1998–January 2002. An overview of the instrument, input data, and processing framework are provided in §2 and §3. In §4, we outline the fire detection algorithm including important considerations that went into defining the science data products described in §5. Finally, in §6, we present the results from our first efforts towards characterizing algorithm performance and validating the VIRS fire products.

2. Instrument

2.1. *TRMM orbit*

The TRMM satellite, launched in November 1997, occupied a 350 km circular orbit inclined at 35° (Kummerow *et al*. 1998). The local overpass time consequently drifts over the entire 24 hours of each day roughly once each month for rainfall monitoring. This is also an attractive aspect of the platform for fire observation as it permits a complete sampling of the diurnal burning cycle. At equatorial latitudes two VIRS observations (spaced about 12 h apart) are typically made every other day; at temperate latitudes two to three VIRS observations (spaced a few hours apart) are made every day. Detailed information about the TRMM orbit is available from the TRMM Science and Data Information System (TSDIS) on-line overflight finder*.

In August 2001 the satellite orbit was boosted to 402.5 km. The implications for VIRS-derived fire products are discussed in §7.

2.2. *VIRS characteristics*

The VIRS has five bands centred at 0.63, 1.61, 3.75, 10.8, and 12.0 μm, designated channels 1–5, respectively. Each detector has a 6.02 mrad field of view, yielding pre-boost trapezoidal pixels nominally 2.1 km in size (2.4 km post-boost) at the Earth's surface (Kummerow *et al*. 1998). Channels 4 and 5 saturate at an equivalent blackbody temperature of 325 K, while channel 3 saturates at a lower 321.2 K.

3. Input data and processing framework

Calibrated VIRS radiance data (1B01) were obtained from the Goddard Earth Sciences Distributed Active Archive Center (GES DAAC). Observations for each orbit are contained in a single file, along with navigation, viewing geometry and comprehensive metadata. For each 1B01 file an intermediate product was generated containing top-of-atmosphere reflectances and brightness temperatures needed by the detection algorithm.

A problematic aspect of the 1B01 product (in the context of fire detection) was that saturated, zero radiance and missing data pixel values were assigned a single missing-data value. As active fires routinely cause saturation of the 3.75 μm

*http://www-tsdis.gsfc.nasa.gov/tsdis/PredictOrbit.html

channel, this would normally render the dataset largely useless for fire detection. For this reason, pre-processing was required to identify and restore saturated pixels. Restoration was based upon examination of neighbouring valid pixels to determine whether or not these were 'warm'; if so, the missing pixel was assumed to be saturated. Since it is far more common for an entire scan to be truly missing rather than just a few pixels within an otherwise valid scan, restoration was not attempted on those scans with no valid observations.

With a data rate of 1.5 GB/day (compressed), management and processing of the VIRS Level 1B01 data product in a timely matter was also problematic. TRMM VIRS data cover the time period from 21 December 1997 to present. For over three years of historical data, the data volume exceeds 1.6 TB. To mitigate the problems associated with managing such a large amount of data, it was decided to participate in the GES DAAC's development of a pilot Knowledge Discovery in Databases (KDD) subsystem (Lynnes and Mack 2001). The DAAC has found that many large-volume users actually seek a relatively small information component within the data, which they extract locally using KDD techniques. To improve the efficiency of this process, the DAAC has implemented a KDD subsystem that supports execution of a user's algorithm at the data centre, dramatically reducing the volume that is sent to the user. The data are extracted from the archive in a planned, organized 'campaign', the algorithms are executed, and the output products sent to the users over the network. By allowing the DAAC to execute the fire detection algorithm code, over three years of VIRS data (1.6 TB) were processed and reduced to a manageable volume of 115 GB in less than two months.

4. Algorithms

4.1. *Cloud and water masking*

Cloud detection was performed using the technique employed in the production of the International Geosphere Biosphere Program (IGBP) AVHRR-derived Global Fire Product (Stroppiana *et al.* 2000). Daytime pixels are considered to be cloud-obscured if the following condition is satisfied:

$$((\rho_1+\rho_2) > 1.2) \text{ or } (T_5 < 265 \text{ K}) \text{ or } ((\rho_1+\rho_2) > 0.8 \text{ and } T_5 < 285 \text{ K})$$

where ρ_1 and ρ_2 are the VIRS channel 1 and 2 reflectances, respectively, and T_5 is the channel 5 brightness temperature. Night-time pixels are flagged as cloud if the single condition $T_5 < 265$ K is satisfied. No changes were made to account for the different spectral regions encompassed by the AVHRR and VIRS channel 2. These criteria were found to be adequate for identifying larger, cooler clouds, but consistently missed small clouds and cloud edges. One advantage, however, was that fire pixels were never observed to have been mistakenly flagged as cloud, a problem that has been experienced with other cloud masking methods (Giglio *et al.* 1999). In addition, the fire detection algorithm is generally very resistant to subpixel cloud-induced false alarms, and this simple cloud detection scheme was therefore sufficient for production of this dataset.

Water pixels were identified with the 1 km Multi-angle Imaging Spectro-radiometer (MISR) Digital Terrain Elevation Data (DTED) Intermediate Dataset (Ritter 1994). To match the coarser resolution of the VIRS more reasonably, water boundaries were expanded by approximately 2 km.

4.2. *Fire detection algorithm*

Fire detection was performed using a modified existing algorithm developed for the AVHRR (Giglio *et al*. 1999) that exploits the strong emission of mid-infrared (-IR) radiation from fires (Dozier 1981, Matson and Dozier 1981). A description of the algorithm is provided in the following paragraphs, where the VIRS channel 3 and 4 brightness temperatures are denoted as T_3 and T_4, respectively, the channel 2 reflectance again denoted as ρ_2, and the brightness temperature difference T_{34} defined as $T_3 - T_4$. The algorithm examines each pixel of the VIRS swathe, and ultimately assigns to each one of the following classes: *missing*, *cloud*, *water*, *non-fire*, *fire* or *unknown*.

Pixels lacking valid data are immediately classified as *missing* and excluded from further consideration. Cloud and water pixels are identified using the previously described cloud and water masks, and are assigned the classes *cloud* and *water*, respectively. The algorithm considers only those clear land pixels that remain. A pixel is identified as a potential fire pixel if $T_3 > 310\,\mathrm{K}$, $T_{34} > 6\,\mathrm{K}$ and $\rho_2 < 0.32$, otherwise it is classified as *non-fire*. (Night-time requirements are $T_3 > 306\,\mathrm{K}$ and $T_{34} > 6\,\mathrm{K}$, with no ρ_2 test.) If the pixel has been identified as a potential fire, an attempt is made to use the neighbouring pixels to estimate the brightness temperatures of the potential fire pixel in the absence of fire. Valid background pixels in a window centred on the potential fire pixel are identified; these are defined as those pixels that (1) contain valid observations, (2) are neither cloud nor water, and (3) are not potential *background* fire pixels. Potential background fire pixels are defined as those background pixels having $T_3 > 318\,\mathrm{K}$ and $T_{34} > 12\,\mathrm{K}$. The window starts as a 5×5 pixel square 'ring' around the potential fire pixel (the eight pixels immediately surrounding the potential fire pixel are excluded). The ring is increased to a maximum of 21×21 pixels, as necessary, until at least 25% of the background pixels within the window are valid, and the number of valid background pixels is at least six. If an insufficient number of valid background pixels is identified, the candidate fire pixel is classified as *unknown*, otherwise the following statistics are computed: T_{34B} and δ_{34B}, the respective mean and mean absolute deviation of $T_3 - T_4$ for the valid background pixels; T_{4B} and δ_{4B}, the respective mean and mean absolute deviation of T_4 for the valid background pixels.

For daytime scenes the following conditions are then evaluated:

$$T_{34} > T_{34B} + 3.5\,\delta_{34B} \tag{1}$$

$$T_{34} > T_{34B} + 6\ \mathrm{K} \tag{2}$$

$$T_4 > T_{4B} + \delta_{4B} - 1.5\ \mathrm{K} \tag{3}$$

For night-time scenes condition (3) is not required. If any condition is not satisfied, the pixel is classified as *non-fire*. If all conditions are satisfied, however, night-time pixels are classified as *fire* and daytime pixels undergo a final Sun-glint rejection test. This is essential due to the wide range of Sun positions experienced by the TRMM satellite. For these daytime pixels, the angle between vectors pointing in the surface-to-satellite and specular reflection directions, θ_g, is calculated, where

$$\cos\theta_g = \cos\theta_v \cos\theta_s - \sin\theta_v \sin\theta_s \cos\phi \tag{4}$$

Here θ_v and θ_s are the view and solar zenith angles, respectively, and ϕ is the

relative azimuth angle. A count is made of adjacent water pixels, i.e. the number of water pixels within the eight pixels surrounding the candidate fire pixel, and is denoted by N_w. The following conditions are then evaluated:

$$\theta_g < 5^\circ \tag{5}$$

$$\theta_g < 15^\circ \text{ and } \rho_2 > 0.2 \tag{6}$$

$$\theta_g < 20^\circ \text{ and } N_w > 0. \tag{7}$$

If one or more of the conditions are satisfied, the fire pixel is rejected as Sun glint and classified as *non-fire*, otherwise it is classified as *fire*.

4.3. *Fire detection confidence*

For each fire pixel a detection confidence estimate is provided. In addition to several of the previously defined variables, it incorporates the background window size L (the background window is $L \times L$ pixels in size), and two standardized variables, z_4 and z_{34}, defined as

$$z_4 = \frac{T_4 - T_{4B}}{\delta_{34B}} \tag{8}$$

$$z_{34} = \frac{T_{34} - T_{34B}}{\delta_{34B}} \tag{9}$$

Both quantities represent the number of absolute deviations that T_4 and T_{34} lie from their respective means, and are analogous to the more commonly used Z-scores.

Our scheme for quantifying fire detection confidence employs a ramp function, defined as:

$$S(x;\alpha,\beta) = \begin{cases} 0; & x \leqslant \alpha \\ (x-\alpha)/(\beta-\alpha); & \alpha < x < \beta \\ 1; & x \geqslant \beta \end{cases} \tag{10}$$

For the daytime detection algorithm, the confidence assigned to each fire pixel is made up of a combination of five sub-confidences, labelled C_1–C_5. Each has a range of 0 (lowest confidence) to 1 (highest confidence), and are defined as:

$$C_1 = S(T_3;\ 310\text{ K}, 321.2\text{ K})$$
$$C_2 = S(T_{34};\ 6\text{ K}, 15\text{ K})$$
$$C_3 = S(z_{34};\ 3.5, 5)$$
$$C_4 = S(z_4;\ -0.5, 0.5)$$
$$C_5 = 1 - S(L;\ 5, 21)$$

For C_1, 310 K is the minimum brightness temperature required for a pixel to be considered a fire pixel (and is thus less obviously a fire), while 321.2 K is the largest brightness temperature that can be expected due to saturation. For C_2, 6 K is the

smallest value of T_{34} required for a pixel to be considered a fire pixel, and, based on operational experience, 15 K represents a typical value for a strong fire. For C_3, $z_{34} = 3.5$ is the minimum value for a fire pixel, and $z_{34} = 5$ is a typical value (again based on operational experience) for an isolated, strong fire pixel. C_4 drops sharply as T_4 falls below the background channel 4 brightness temperature, and indication that the fire pixel might be an undetected cloud pixel. Finally, C_5 reduces the confidence as the size of the background window grows larger, accounting for the fact that the characterization of the local background is less likely to be representative as the distance from the candidate fire pixel increases. From these individual sub-confidences, the daytime summary detection confidence C is then defined as their geometric mean

$$C = \sqrt[5]{C_1 C_2 C_3 C_4 C_5} \tag{11}$$

which possesses the property of having a value of zero if any of the sub-confidences is zero. Alternative combinations include the arithmetic mean and the product of the sub-confidences. With the former, low individual sub-confidences penalize C mildly; with the latter they penalize C very heavily. The geometric mean lies between these two extremes.

For the night-time detection algorithm C_4 is omitted entirely and the lower threshold α of C_1 is instead 306 K. The night-time detection confidence is then the geometric mean of C_1, C_2, C_3 and C_5.

5. Product description

5.1. *General description and considerations*

Three types of fire products were generated as part of this activity: an individual orbit-level fire product, a daily 0.5° 'global' fire product, and a 0.5° global monthly fire summary dataset. The first two are primarily intermediate products used to produce the monthly fire product, and as such will not be described in detail.

Each orbit-level product is generated from a single 1B01 input file, and contains an active-fire mask and a table of information about each fire pixel (location, radiometric properties, etc.). Each day's orbits are used to produce a global daily fire product, 'global' being used here to mean all fires detected in the TRMM VIRS geographical range of observation (38° S to 38° N). The coarse-resolution, gridded monthly product is more appropriate for many purposes. As a monthly product, it offers the advantage of a more representative sampling of the diurnal burning cycle that is not provided in individual orbit-level or daily products.

In producing a gridded, temporally composited active fire dataset, ideally one must compensate for various biases that can be introduced in the process. One of the more significant sources is the multiple observation of the same fire over successive satellite overpasses. This will bias fire counts upward in regions of more frequent observation, and is generally a more serious issue for fire counts derived from the VIRS due to the highly-inclined TRMM orbit. This oversampling also affects fire products derived with polar-orbiting platforms such as the AVHRR, ATSR and MODIS, but has largely been ignored in previous work. Other bias sources include variable cloud cover and missing observations. Biases can also be introduced by the detection algorithm itself, in terms of both missed fires and false detections, and are dependent upon viewing geometry, biome, season and other factors (Giglio *et al.* 1999).

5.2. *Product data layers*

The monthly product consists of 14 separate data layers. Twelve of these are 160 row by 720 column images covering the Earth's surface between latitudes 40° S to 40° N with 0.5° equal-angle bins. These image layers contain raw and corrected pixel counts, land-cover information and some quality assurance-related fields. Additional specialized layers are stored in a more compact table format. Examples of three product layers are shown in figure 1, and a description of each layer is provided below.

In the following discussion we refer to the fraction of the grid cell at (i,j) overlapped (or covered) by the kth orbit swathe as the *coverage fraction*, and denote it by $c_k(i,j)$, where $0 \leqslant c_k(i,j) \leqslant 1$. This quantity is important due to the difference in pixel size at different parts of the VIRS scan. The coverage fraction is used to compensate for the fact that different overpasses may overlap the same fraction of a particular grid cell, yet the number of pixels falling within the cell from each swathe may differ significantly. In our implementation, it was computed using a high-resolution grid nested within each coarse-resolution grid cell. To simplify notation, the index of all summations appearing in the following equations is not shown explicitly but understood to be k.

Raw fire pixels. The total number of active fire pixels was detected in each grid cell over the entire month, denoted by $N_{\text{fire}}(i,j)$ This layer is the traditional 'gridded fire counts'; as discussed in §5.1, it is biased for several reasons.

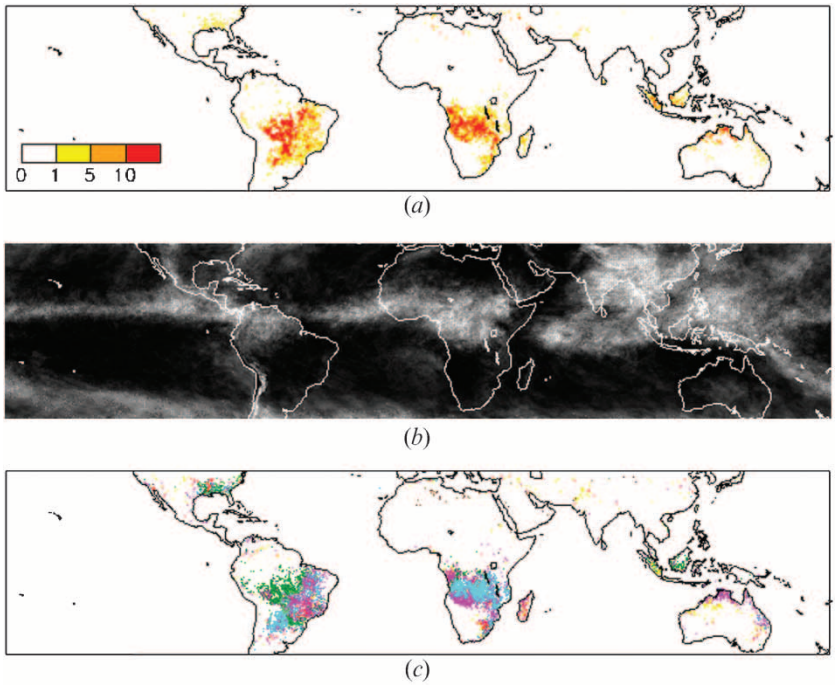

Figure 1. Three data layers from August 1999 tropical active fire product: (*a*) corrected fire pixels; (*b*) mean cloud fraction [range (0,1) shaded between pure black and pure white]; and (*c*) predominant Hansen *et al.* 2000 fire-pixel land cover type (woodland shown in cyan, wooded grassland shown in magenta, forest types shown in various shades of green).

Corrected fire pixels. The total number of fire pixels observed in each grid cell was corrected for multiple satellite overpasses and missing observations. This is accomplished by normalizing the raw fire pixel counts to the equatorial coverage in a full month containing no missing observations. Specifically, the corrected fire pixel count, denoted by $N'_{\text{fire}} = (i,j)$, is given by

$$N'_{\text{fire}}(i,j) = \frac{N_{\text{days}} \bar{c}_{\text{eq}} \sum N_{\text{fire},k}(i,j)}{\sum c_k(i,j)} \tag{12}$$

where N_{days} is the number of days in the particular month for which the product is being generated and $\bar{c}_{\text{eq}}$ is the ideal average daily equatorial grid cell coverage. The latter quantity is the average fraction of the equator that is covered by the VIRS swathe each day. For an orbit inclination of γ and a swathe width of w, it is given by

$$\bar{c}_{\text{eq}} = \frac{w\,N}{\pi\,R_{\text{E}} \sin\gamma} \tag{13}$$

where R_{E} is the radius of the Earth and N is the number of orbits each day. Inserting values appropriate for the TRMM satellite and the VIRS instrument following the orbit boost ($\gamma = 35^{\circ}$, $w = 830\,\text{km}$, $N \approx 15.6$) yields $\bar{c}_{\text{eq}} \approx 1.13$.

Fire pixel density. The density of corrected fire pixel counts within each grid cell in km^{-2} was denoted by σ_{fire} and defined as

$$\sigma_{\text{fire}} = \frac{N'_{\text{fire}}(i,j)}{f_{\text{land}}(i,j) A_{\text{cell}}(i)} \tag{14}$$

where $f_{\text{land}}(i,j)$ is the land fraction of the grid cell at (i,j) and $A_{\text{cell}}(i)$ is the grid cell area (which is solely a function of i due to the equal-angle grid used to composite pixels). The fire pixel density is defined only for those cells in which $f_{\text{land}}(i,j) > 0$; it is included to allow an unbiased visual interpretation by compensating for the apparent reduction in fire pixel counts at higher latitudes (a consequence of the equal-angle grid used for the product).

Mean cloud fraction. The average fraction of each grid cell obscured by cloud over the entire month can be useful for deriving additional high-level products. It is computed from the cloud fractions $f_{\text{cloud},k}(i,j)$ of the individual orbit swathes that overlap each cell, where $\text{f}_{\text{cloud},k}(i,j) = \text{N}_{\text{cloud},k}(i,j)/\text{N}_{\text{total},k}(i,j)$. The mean cloud fraction is then the average of the cloud fractions for each overpass, weighted by the cell coverage:

$$\bar{f}_{\text{cloud}}(i,j) = \frac{\sum f_{\text{cloud},k}(i,j) c_k(i,j)}{\sum c_k(i,j)} \tag{15}$$

Cloud-corrected fire pixels. The total number of fire pixels observed in each grid cell were corrected for multiple satellite overpasses, missing observations, and variable cloud cover. This correction is based upon the assumption that the rate of fire occurrence within both clear and cloud-obscured areas is the same, which may or may not be reasonable (Eva and Lambin 1998). The quantity is nevertheless included as part of the product to provide an upper limit on fire activity. The cloud-corrected fire pixel count, denoted by $N''_{\text{fire}}(i,j)$, is given by

$$N''_{\text{fire}}(i,j) = \frac{N'_{\text{fire}}(i,j)}{1 - f_{\text{cloud}}(i,j)} \tag{16}$$

In the event the mean cloud fraction is unity [which also implies that $N_{\text{fire}}(i, j)$], the cloud-corrected fire pixel count is undefined and assigned a value of zero.

Mean detection confidence. The mean detection confidence of all fire pixels detected within each grid cell is included primarily for quality assurance.

Fire-pixel land cover statistics. For each grid cell, the fraction of fire pixels within each of the land cover classes were obtained from the University of Maryland Laboratory for Global Remote Sensing Studies 1 km land cover product (Hansen *et al*. 2000). To reduce storage requirements, this layer is stored as a compact table.

Fire-pixel predominant land cover type. The predominant land-cover type of all fire pixels within the grid cell was determined using the mode of land-cover classes for all fire pixels within each cell. A summary of the previous layer is in a simpler image format.

Volcano layers. Tables of volcanoes that appeared to be active during the month, and affected grid cells are included. A comparison of fire-pixel locations with an external database (Simkin and Siebert 1994) was used to identify volcanic sources. These layers allow users to investigate volcanic activity and remove potentially misleading non-fire 'hot spot' sources if desired.

Additional data layers. Additional layers containing simple counts of missing, unknown and total pixels are included to assist quality assurance and simplify the production of experimental high-level datasets. Counts of missing and *unknown* class pixels are useful for identifying large areas of saturation, such as deserts, in which the algorithm becomes incapable of detecting fires.

6. Algorithm performance and product evaluation

Two independent methods were employed to assess algorithm performance and evaluate the fire products. First, simulated VIRS imagery was used to quantify algorithm detection and false alarm rates under a wide range of environmental conditions within different biomes. Second, active fire pixels within images from selected locations were manually identified and compared to fire pixels detected by the algorithm. The use of two independent methods for product evaluation was intended to help offset the inherent limitations of each.

6.1. *Simulated fire scenes*

6.1.1. *Method*

Simulated VIRS channel 3 and 4 scenes were generated using a modification of the method used by Giglio *et al*. (1999) for the evaluation of several AVHRR active fire detection algorithms. These scenes contained idealized fires of various sizes and temperatures in 13 tropical and subtropical biomes. The fire detection algorithm was applied to the simulated VIRS imagery and its performance was characterized in terms of probability of fire detection (P_d) and false alarm (P_f) as functions of fire temperature and area, solar and viewing geometry, visibility, season and biome.

This approach allows complete knowledge of all components within every scene, permitting algorithm performance to be determined over the widest possible range of fire and environmental conditions. It is also inherently less realistic, however, being limited by, among other things, assumptions within the model, imperfect knowledge of parameters required by the model, and the model itself. Nevertheless, the simulation approach to algorithm and product evaluation can provide useful information, albeit coarse, to guide the use of the data.

6.1.2. *Results*

Because the probability of detection (P_d) is so strongly dependent upon the temperature and area of the fire being observed, P_d is summarized as a *detection matrix* in which fire temperature and area form the rows and columns of the matrix. Such matrices are shown graphically in figure 2.

For the biomes considered, the 'envelope' of detection (i.e. the range of fire sizes and temperatures having non-zero P_d) is generally comparable. The size of the smallest flaming fire having a reasonable chance of being detected by VIRS under ideal conditions, defined as $P_d \geqslant 0.3$, was between 100–200 m^2. Within this range, P_d rises to 1, and remains fixed with increasing fire temperature and/or area until saturation in the mid-IR channel ultimately drives P_d back to 0 (Giglio *et al.* 1999). Purely smouldering fires must be ~ 10 times larger to achieve a similar probability of detection.

An exception occurs in dry-season tropical savanna (wooded grassland in the Hansen *et al.* 2000 classification) during the day for solar zenith angles below $\approx 50^\circ$. For this case, the envelope of detection was much smaller than all of the other biomes modelled, and the probability of detection never exceeded ≈ 0.5. This relatively poor performance is caused by frequent mid-IR channel saturation, in turn the result of elevated surface temperatures and the prominent reflected solar radiation accompanying the exposed soil and senescent vegetation of this biome. Under these conditions, the contrast between active fires and the background surface is substantially reduced, and the algorithm is largely incapable of detecting fires (indeed, with the Sun directly overhead P_d is uniformly 0).

In the simulation, no false detections were observed under any circumstances, including coastal and dry-season tropical savanna scenes for which the original AVHRR-tuned algorithm produced false alarms during the day at solar zenith

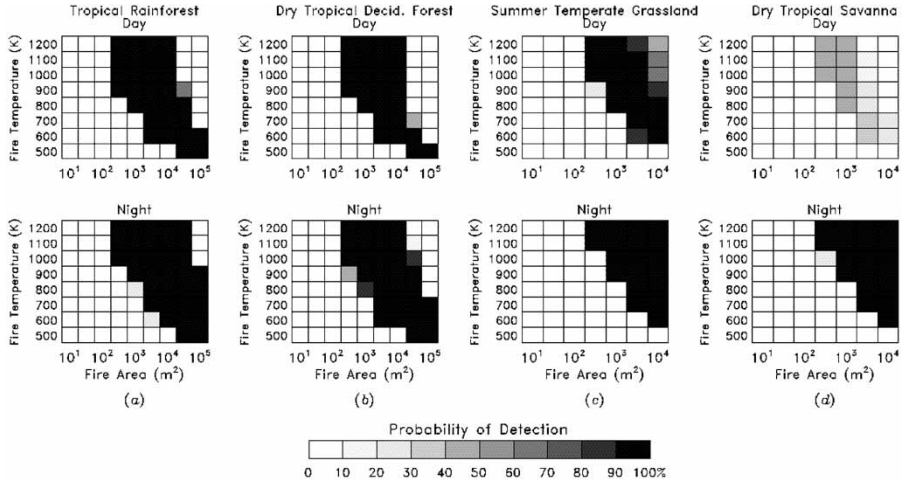

Figure 2. Pre-boost daytime (top row) and night-time (bottom row) detection matrices for various biomes: (*a*) tropical rainforest with 0° scan angle, 0° solar zenith angle (daytime case); (*b*) dry-season tropical deciduous forest with 0° scan angle, 0° solar zenith angle (daytime case); (*c*) summer temperate grassland with 0° scan angle, 40° solar zenith angle (daytime case); and (*d*) dry-season tropical savanna with 0° scan angle, 40° solar zenith angle (daytime case).

angles below 30° (Giglio *et al*. 1999). This was expected, as the simulation itself was used, in conjunction with extensive operational testing, to alter the original AVHRR-specific thresholds for the VIRS algorithm. In addition, several years of operational experience have demonstrated that this simulation underestimates false alarm rates. As such, a valid goal in tuning the algorithm is to require the simulation-derived false alarm rates to be *zero*.

6.2. *Visual inspection of VIRS scenes*

6.2.1. *Method*

In the second approach, images from selected evaluation sites were manually examined to identify active fires for comparison with fire pixels detected by the algorithm. Based upon experience with different sensors and fire detection algorithms, regions in which both true fires and false alarms occur were chosen and are shown in figure 3. For each of the evaluation sites, images from days randomly selected in each month of the 1998–1999 dataset were prepared; these contained all channels present in the intermediate 1B01 product described in §3, and the active-fire mask produced by the fire detection algorithm.

Unambiguous and ambiguous fire pixels in each image were identified by visual inspection. In daytime scenes, unambiguous active fire pixels were frequently accompanied by an obvious smoke plume, and sometimes a large adjacent burn scar, identifiable in the visible and short-wave IR channels. Ambiguous fire pixels included those that appeared to contain active fires but which lacked unequivocal evidence such as a smoke plume or night-time mid-IR saturation.

For each image, manually identified fire pixels were stored in an 'expert' fire mask. These were then compared to the fire masks generated by the detection algorithm and used to produce truth tables characterizing algorithm performance at each evaluation site. The presence of pixels that cannot be conclusively identified by an expert, i.e. the 'ambiguous fire pixels', means that only upper and lower limits for the probability of detecting a fire (P_d) and the probability of a false alarm (P_f) may be computed (rather than a single representative value of P_d and P_f for each site). These limits are denoted $P_{d,max}$ and $P_{d,min}$, the respective upper and lower limits of P_d, and $P_{f,max}$ and $P_{f,min}$, the respective upper and lower limits of P_f.

To calculate the above limits, seven quantities are required for each evaluation site. The first six are the elements of the truth table containing the numbers of pixels within the different classes assigned by the detection algorithm and the expert (table 1); these are denoted by $M_{n,n}$, $M_{n,a}$, $M_{n,u}$, $M_{f,n}$, $M_{f,a}$ and $M_{f,u}$. For these

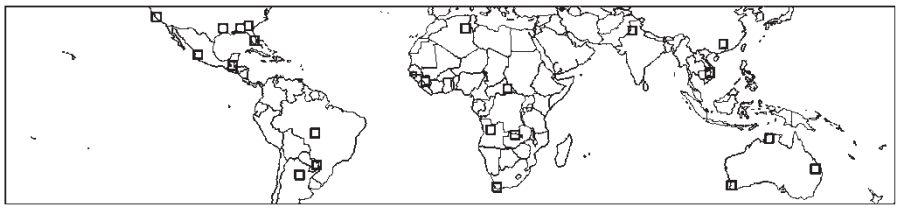

Figure 3. Locations of the 22 product evaluation sites. Regions in which true fires and false alarms could be expected were selected on the basis of experience with multiple sensors and detection algorithms. The Algerian site contained small gas flares.

Table 1. Elements of truth table used to calculate limits of detection and false alarm probabilities. The first subscript denotes the class assigned to a pixel by the algorithm; the second denotes the class assigned by the expert.

	Expert class		
Algorithm class	Non-fire	Ambiguous fire	Unambiguous fire
Non-fire	$M_{n,n}$	$M_{n,a}$	$M_{n,u}$
Fire	$M_{f,n}$	$M_{f,a}$	$M_{f,u}$

variables, the first subscript indicates the class assigned by the detection algorithm [*non-fire* (n) or *fire* (f)], and the second indicates the class assigned by the expert: *non-fire* (n), *ambiguous fire* (a), or *unambiguous fire* (u). Finally, the number of clear land pixels for all images at each site, M_{clear}, is also needed. It is used in place of the *total* number of pixels at each site because the detection algorithm was not applied to water or cloud pixels.

In this evaluation, pixels assigned a class of *unknown* were reclassified as *non-fire* pixels. Although a third row could have been included in the truth table to accommodate such pixels, the total number encountered in this class was negligible ($\sim$100 for all sites combined). In addition, operational experience has shown that nearly all pixels assigned a class of *unknown* are in fact not active fires, thus it is more sensible to treat them as non-fire pixels in this analysis.

The minimum probability of false alarm occurs when all ambiguous fire pixels *are* true fires, and the maximum probability of false alarm occurs when all ambiguous fire pixels *are not* true fires. Using the notation described previously, the lower and upper limits for P_f are:

$$P_{f,min} = M_{f,n}/M_{clear} \tag{17}$$

$$P_{f,max} = (M_{f,n} + M_{f,a})/M_{clear} \tag{18}$$

The minimum probability of detection occurs when, of all ambiguous fire pixels, those *undetected* by the algorithm are in fact true fires:

$$P_{d,min} = M_{f,u}/(M_{n,a} + M_{n,u} + M_{f,u}) \tag{19}$$

The maximum probability of detection occurs when, of all ambiguous fire pixels, those *detected* by the algorithm are in fact true fires:

$$P_{d,max} = (M_{f,a} + M_{f,u})/(M_{f,a} + M_{n,u} + M_{f,u}) \tag{20}$$

Over 500 images were analysed in this manner. To account for the different day and night algorithm modes (§4.2), separate daytime and night-time statistics were generated. Compared to the simulation approach, this evaluation method offers greater realism, at the expense of complete knowledge of each scene and comprehensive sampling of the various environmental conditions that may be encountered.

Table 2. Daytime evaluation summary.

Location	Clear land pixels (M_{clear})	Unambiguous fire pixels	Ambiguous fire pixels	Detected unambiguous fire pixels ($M_{f,u}$)	Detected ambiguous fire pixels ($M_{f,a}$)	False fire pixels ($M_{f,n}$)	P_d		P_f	
							Min.	Max.	Min.	Max.
Algeria	165 715	33	56	6	0	0	0.07	0.81	0	0
Angola	205 794	1256	1298	577	104	15	0.23	0.50	7.3×10^{-5}	5.8×10^{-4}
N. Argentina	429 962	50	108	22	26	0	0.17	0.63	0	6.0×10^{-4}
E. Australia	228 167	16	32	16	12	0	0.44	1.0	0	5.3×10^{-5}
N. Australia	207 656	76	65	49	29	9	0.44	0.74	4.3×10^{-5}	1.8×10^{-4}
W. Australia	225 431	55	108	36	19	1	0.25	0.74	4.4×10^{-6}	8.9×10^{-5}
Brazil	188 901	106	135	90	66	7	0.51	0.91	3.7×10^{-5}	3.9×10^{-4}
CAR	290 843	664	568	227	106	12	0.20	0.43	4.1×10^{-5}	4.1×10^{-4}
China	210 417	9	5	9	2	1	0.75	1.0	4.8×10^{-6}	1.4×10^{-5}
Guatemala	161 361	368	441	238	88	7	0.33	0.71	4.3×10^{-5}	5.9×10^{-4}
Guinea	293 681	243	555	181	95	18	0.26	0.82	6.1×10^{-5}	3.8×10^{-4}
N. India	404 113	2	11	2	5	3	0.25	1.0	7.4×10^{-6}	2.0×10^{-5}
Mexico	232 338	30	31	21	21	3	0.52	0.82	1.3×10^{-5}	1.0×10^{-4}
Paraguay	280 853	190	459	145	177	15	0.31	0.88	5.3×10^{-5}	6.8×10^{-4}
South Africa	272 361	12	15	10	2	0	0.40	0.86	0	7.3×10^{-6}
South-east Asia	319 401	48	123	34	50	2	0.28	0.86	6.3×10^{-6}	1.6×10^{-4}
USA, Alabama	506 097	9	6	5	0	1	0.33	0.56	2.0×10^{-6}	2.0×10^{-6}
USA, Georgia	629 512	3	9	3	7	1	0.60	1.0	1.6×10^{-6}	1.3×10^{-5}
USA, Florida	204 797	18	15	16	8	0	0.64	0.92	0	3.9×10^{-5}
USA, Texas	553 460	38	24	30	12	3	0.60	0.84	5.4×10^{-6}	2.7×10^{-5}
USA, California	323 704	10	10	10	10	0	1.0	1.0	0	3.1×10^{-5}
Zambia	469 907	963	1469	518	172	28	0.23	0.61	6.0×10^{-5}	4.3×10^{-4}

CAR = Central African Republic.

Table 3. Night-time evaluation summary.

Location	Clear land pixels (M_{clear})	Unambiguous fire pixels	Ambiguous fire pixels	Detected unambiguous fire pixels ($M_{f,u}$)	Detected ambiguous fire pixels ($M_{f,a}$)	False fire pixels ($M_{f,n}$)	P_d		P_f	
							Min.	Max.	Min.	Max.
Algeria	327 460	38	73	34	6	0	0.32	0.91	0	1.8×10^{-5}
Angola	261 860	42	25	20	0	0	0.30	0.48	0	0
N. Argentina	290 145	16	34	14	0	0	0.28	0.88	0	0
E. Australia	378 395	17	31	15	0	0	0.31	0.88	0	0
N. Australia	223 593	75	148	52	5	0	0.24	0.71	0	2.2×10^{-5}
W. Australia	505 728	9	16	3	0	0	0.12	0.33	0	0
Brazil	199 449	98	160	75	10	0	0.30	0.79	0	5.0×10^{-5}
CAR	111 936	318	419	177	0	0	0.24	0.56	0	0
China	186 412	0	2	0	0	0	0.00	–	0	0
Guatemala	111 194	5	3	5	0	0	0.62	1.00	0	0
Guinea	138 078	14	19	9	4	0	0.31	0.72	0	2.9×10^{-5}
N. India	182 177	0	0	0	0	0	–	–	0	0
Mexico	169 245	5	2	5	0	0	0.71	1.00	0	0
Paraguay	156 693	3	8	3	0	0	0.27	1.00	0	0
South Africa	249 864	0	0	0	0	0	–	–	0	0
South-east Asia	130 736	39	9	32	6	0	0.76	0.84	0	4.6×10^{-5}
USA, Alabama	436 637	1	5	1	0	0	0.17	1.00	0	0
USA, Georgia	239 510	0	0	0	0	0	–	–	0	0
USA, Florida	124 964	0	0	0	0	0	–	–	0	0
USA, Texas	508 037	11	8	11	2	0	0.65	1.0	0	3.9×10^{-6}
USA, California	239 849	4	2	4	0	0	0.67	1.0	0	0
Zambia	397 748	10	22	4	0	0	0.12	0.40	0	0

CAR = Central African Republic.

Table 4. Evaluation site summary. University of Maryland land cover classes are listed in order of composition; first is primary.

Site location	Scene land cover primary components	Algorithm-detected fire land cover (where different from scene)
Algeria	bare ground	
Angola	woodland	
N. Argentina	woodland, wooded grassland	
E. Australia	wooded grassland, woodland	
N. Australia	wooded grassland	
W. Australia	cropland, woodland, broadleaf evergreen forest	woodland, broadleaf evergreen forest
Brazil	broadleaf evergreen forest	
CAR	woodland	
China	grassland, wooded grassland	cropland, grassland
Guatemala	broadleaf deciduous forest	
Guinea	wooded grassland, woodland	
N. India	cropland	grassland
Mexico	woodland, wooded grassland	
Paraguay	broadleaf evergreen forest	
South Africa	cropland, woodland	wooded grassland, closed shrubland
South-east Asia	woodland, broadleaf evergreen forest	woodland, wooded grassland
USA, Alabama	woodland, cropland	
USA, Georgia	woodland, cropland	
USA, Florida	wooded grassland, cropland	woodland, wooded grassland
USA, Texas	woodland, wooded grassland, cropland	needleleaf evergreen forest, woodland
USA, California	cropland, wooded grassland	grassland, closed shrubland, woodland
Zambia	woodland	

CAR = Central African Republic.

6.2.2. *Results*

Tables 2 and 3 summarize the day and night-time performance of the VIRS algorithm, in terms of fire detection and false alarm statistics, for each evaluation site analysed using the visual inspection method. Table 4 shows a characterization of the evaluation sites using the Hansen *et al.* (2000) 1 km land cover classification. Overall, the results shown in table 2 indicate at least a moderate probability of detection during the day (i.e. P_d values greater than 0.6 fall within the range reported) for almost all sites examined. Generally, the higher daytime probabilities of detection ($P_{d,min} > 0.6$) were observed in sites with the primary land cover being non-forest classes (e.g. wooded grassland and cropland) where a sizeable portion of the fire activity ($> 30\%$) occurred in grassland or cropland pixels.

In contrast, the lower probabilities of fire detection ($P_{d,min} \leqslant 0.3$) were almost always observed in sites characterized as predominantly forest or woodland, where the fire activity *also* occurred primarily ($> 80\%$) in forest or woodland pixels. Included in this group are the sites in central Africa (Central African Republic, Angola, Zambia) that demonstrated some of the highest fire activity observed. Of the 22 evaluation sites examined, seven exhibited high levels of fire activity, with at least 100 unambiguous fires counted by the expert. In all but one of the high fire activity sites, the predominant land cover type was forest or woodland. The exception is the Guinea site in West Africa which contains mixed grassland and

woodland pixels, with 79% of the visually identified unambiguous fire pixels falling in non-forest or woodland classes.

At first glance, this result may appear to be somewhat contradictory to the simulation results, i.e. that a lower P_d may be expected for fires in dry season tropical savanna than in tropical forest biomes. However, contamination of the background characterization by undetected fires, a scenario that is much more likely as fire activity increases in a region, was shown to reduce significantly the probability of detection for contextual algorithms (Giglio *et al*. 1999).

The poorest algorithm performance was exhibited at the Algeria site. Characterized as bare ground in the Hansen *et al*. (2000) classification, this site exhibited extremely low P_d (range 0.07–0.08) during the day, but night-time values nore comparable to the other sites. This result is expected as the fires observed in this region, always present at the same locations, are gas flares—small intense fires that show very low contrast to the background surface elements that are very bright and hot during the day.

Overall, the probability of false alarm was $\sim 10^{-5}$ for clear land pixels. It is instructive to evaluate this quantity in terms of the total number of false alarms which might be expected. Assuming a typical mean cloud fraction of ≈ 0.4, and that half of the $\sim 1.9 \times 10^7$ VIRS land pixels observed each day are made at night (for which $P_f = 0$), we obtain a rough estimate for the number of false fire pixels each day of ~ 60. This corresponds to less than 10% of the ~ 700 fire pixels detected on average each day. The surface features and observation conditions that cause false alarms for this type of detection algorithm (e.g. land cover type boundaries, Sun glint over land or a small inland waterbody, etc.) occur in all geographical regions. As expected, no obvious geographical or land cover trend was found during the evaluation. The false alarm rates observed were consistent across different regions, with the lowest possible range of P_f found for sites in the more temperate regions (US, India). The highest upper limit of P_f was observed for the Paraguay site.

The fire activity observed for most sites, both with the algorithm and by visual inspection, was significantly lower at night. However, in four of the 22 evaluation sites, there was no unambiguous night-time fire activity observed at all, making a comparison between day and night algorithm performance impossible. In the 12 sites where the comparison can be made, the differences in performance observed present no clear trends related to vegetation characterization or changes in fire activity from day to night. Not surprisingly, the probability of a night-time false alarm was effectively zero at all locations. This was expected as most false fire pixels are caused by reflected mid-IR solar radiation.

The visual inspection evaluation technique suffers from two significant deficiencies. First, there is a nontrivial degree of subjectivity in this type of analysis caused by ambiguities within individual scenes. One example is small apparent fires not accompanied by visible smoke plumes (such fires occur frequently in central and southern Africa, for example). Such detections may in fact be false alarms, such as sunlight reflected from a small inland waterbody (not identified in the 1 km water mask), and different analysts may lump such pixels into either category. Secondly, one has no knowledge of the instantaneous fire properties. Below a certain size and temperature, an active fire will yield a satellite-based measurement too weak for even an expert observer to identify. Smoke and clouds may sometimes render even very large, intense fires ambiguous from space. With this technique, therefore, one is limited to estimating an 'average' probability of detecting active fires that are

sufficiently intense and unambiguous that they can be identified from the data themselves by a human expert. Nevertheless, this technique yields at least some measure of algorithm and product performance, and allows identification of potential problems with automated detection algorithms.

7. Impact of the TRMM orbit boost

In August 2001 the TRMM satellite was boosted from its nominal altitude of 350 km to 402.5 km to extend the lifetime of the satellite. Consequences of this change include: (1) an increase in the satellite orbital period by ≈ 1 min; (2) an increase in the VIRS swathe width from 720 km to 830 km; and (3) an increase in the VIRS nadir pixel size from 2.1 km to 2.4 km. The first two changes were accommodated by the correction contained in equations (12) and (13). The change in pixel size, however, is more problematic in the context of maintaining a continuous monthly fire product. The probability of detecting a fire is strongly dependent upon the relative size of the fire within the pixel. An increase in pixel size could therefore introduce discontinuities in the numbers of fires observed before and after the increase, possibly preventing a valid temporal comparison of the monthly fire product spanning the August 2001 orbit boost.

To investigate the impact of the orbit boost on the fire product, we employed the simulation described in §6.1.1 to model post-boost VIRS scenes. As expected, the increase in pixel size increased both the minimum *and* maximum sizes and temperatures of detectable fires, effectively shifting the detection envelopes toward hotter and larger fires. Figure 4 shows results for four of the biomes considered. In general, both the minimum and maximum detectable fire size increased by roughly 20%. In addition, for many fires the probability of detection in the dry season tropical savanna increased slightly ($\approx 10\%$) due to less-frequent saturation. Overall, the difference in pre- and post-boost detection envelopes is small, and the impact of the orbit boost is confined to the edges of the original, pre-boost detection

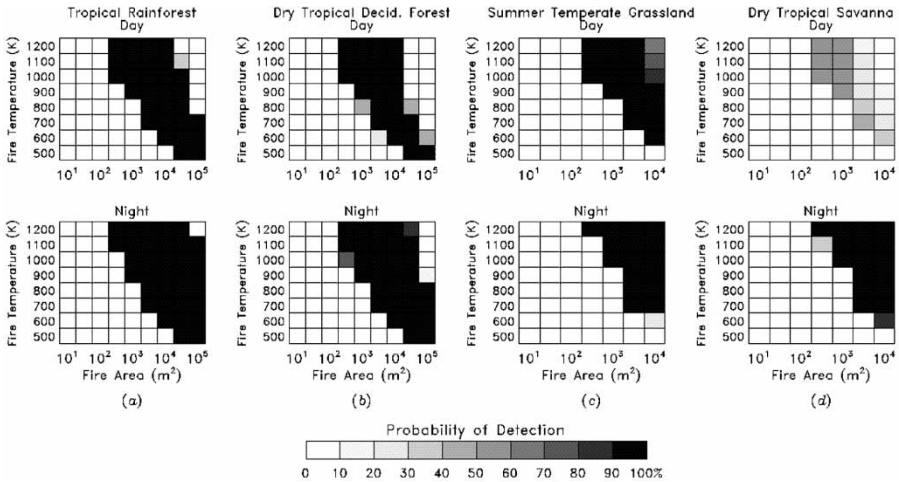

Figure 4. Post-boost daytime (top row) and night-time (bottom row) detection matrices for various biomes under the same viewing conditions used in figure 2: (*a*) tropical rainforest; (*b*) dry-season tropical deciduous; (*c*) summer temperate grassland; and (*d*) dry-season tropical savanna.

envelopes. Although a strict assessment requires *a priori* knowledge of the distribution of instantaneous fire temperatures and areas in each biome—information currently unavailable and impossible to estimate with sufficient accuracy for this application using existing space-borne sensors (Giglio and Kendall 2001)—operationally this should translate into a very small number of affected fires. We therefore expect the impact on the monthly fire product to be negligible. A long-term investigation that includes a time series analysis and comparison with fire products derived from other sensors is underway to confirm this expectation.

8. Conclusion

Results from evaluation of the algorithm presented in this paper indicate that a reasonable active fire product can be systematically generated using observations by the VIRS instrument. As such, efforts to apply the algorithm to the complete current VIRS archive will continue, enabling the generation and distribution of a more than five-year pan-tropical fire product before the end of the TRMM mission in 2004 (or later). As of July 2002, half-degree gridded monthly fire data products for January 1998 through June 2002 have been prepared.

Since the tropical regions present some of the greatest uncertainties in estimates of biomass burning emissions, the new VIRS dataset offers an excellent opportunity to jump start the development of fire data assimilation methodology appropriate for global models prior to the availability of continuous multi-year global fire data from the MODIS instrument on EOS-Terra and EOS-Aqua. For example, this dataset is currently being used to support the atmospheric chemistry modelling activities of the NASA Interdisciplinary Science (IDS) Team working on 'Continued Development and Application of Data Assimilation Techniques for Tropospheric Chemistry Studies'. The VIRS-derived information on location and timing of actual biomass burning will be incorporated into the models being developed in this study to better characterize temporal and spatial variations in tropospheric CO emissions. Even after the availability of global fire data from MODIS, products derived from VIRS will remain useful because of its sampling of the fire diurnal cycle. As described by Eva and Lambin (1998), estimates of regional fire activity based solely on observations made at a specific time each day (as is the case with MODIS and any other instruments residing on Sun-synchronous spacecraft) may be highly biased. It may be feasible to calibrate such products with diurnal observations from VIRS.

Efforts to validate the current VIRS fire product and to develop additional data layers are underway. Alternative approaches to product evaluation are being explored. One such approach is comparison to coincident, high-resolution imagery collected from aircraft and/or satellite-based sensors. The goal of this approach is to gain improved characterization of the fires and fire scenarios that the VIRS instrument (and a particular algorithm applied to VIRS) can 'see'. High spatial resolution observations may provide some details about the instantaneous fire conditions at the surface, potentially allowing estimates of instantaneous fire size and a distinction between flaming and smouldering components (within the fire pixel) to be made. The retrieval of instantaneous fire properties from high-resolution sensors has been previously attempted (Riggin *et al.* 1993, Green 1996). However, this was not done in the context of validating fire products derived from coarser resolution imagery. In practice, such a comparison is greatly complicated by

stringent image coregistration requirements, a need to compensate for sensor differences, and the difficulty in obtaining coincident imagery.

Opportunities for comparing the VIRS product with high-resolution observations of fire from the Advanced Spaceborne Thermal Emission and Reflection Radiometer (ASTER), the MODIS Airborne Simulator (MAS), and the Airborne Visible/Infrared Imaging Spectrometer (AVIRIS) exist, but the technical and practical feasibility of these comparisons has not yet been determined. Acquiring and processing these data is a costly proposition, and in many regions they are only available for a limited number of fires. Therefore, improved modelling may be a more practical alternative for continued VIRS product evaluation. Currently, improved model surfaces are being developed to broaden the regime in which the simulation can more realistically predict false alarm rates, including non-vegetated surfaces (urban or natural) and interfaces between different land-cover types.

Acknowledgments

This work was funded in part by NASA ESE (NRA 99-OES-04). We thank Chris Lynnes (NASA) and the GES DAAC for facilitating the timely production of this dataset. We also thank Prasad Kasibhatla (Duke University), Jennifer Logan (Harvard University), Daniel Jacob (Harvard University), Jacques Descloitres (University of Maryland), Compton Tucker (NASA) and Chris Justice (University of Maryland) for helpful technical discussions.

References

ARINO, O., SIMON, M., PICCOLINI, I., and ROSAZ, J. M., 2001, The ERS-2 ATSR-2 World Fire Atlas and the ERS-2 ATSR-2 World Burnt Surface Projects. *Proceedings of the 8th ISPRS Conference on Physical Measurements and Signatures in Remote Sensing, Aussois, 8–12 January 2001*.

DOZIER, J., 1981, A method for satellite identification of surface temperature fields of subpixel resolution. *Remote Sensing of Environment*, **11**, 221–229.

EVA, H., and LAMBIN, E. F., 1998, Remote sensing of biomass burning in tropical regions: sampling issues and multisensor approach. *Remote Sensing of Environment*, **64**, 292–315.

GIGLIO, L., and KENDALL, J. D., 2001, Application of the Dozier retrieval to wildfire characterization: a sensitivity analysis. *Remote Sensing of Environment*, **64**, 34–49.

GIGLIO, L., KENDALL, J. D., and JUSTICE, C. O., 1999, Evaluation of global fire detection algorithms using simulated AVHRR infrared data. *International Journal of Remote Sensing*, **20**, 1947–1985.

GIGLIO, L., KENDALL, J. D., and TUCKER, C. J., 2000, Remote sensing of fires with the TRMM VIRS. *International Journal of Remote Sensing*, **21**, 203–207.

GREEN, R. O., 1996, Estimation of biomass fire temperature and areal extent from calibrated AVIRIS spectra. *Summaries of the Sixth Annual JPL Airborne Earth Science Workshop*, JPL Publication 96–4, vol. 1, pp. 105–113.

HANSEN, M. C., DEFRIES, R. S., TOWNSHEND, J. R. G., and SOHLBERG, R., 2000, Global land cover classification at 1 km spatial resolution using a classification tree approach. *International Journal of Remote Sensing*, **21**, 1331–1364.

JUSTICE, C. O., and KORONTZI, S., 2000, Global change research requirements for operational satellite fire information from the Global Observation of Forest Cover program. In *Forest Fire Monitoring and Mapping: A component of global observation of forest cover* (Ispra: European Commission), pp. 67–72.

JUSTICE, C. O., VERMOTE, E., TOWNSHEND, J. R. G., DEFRIES, R., ROY, D. P., HALL, D. K., SALOMONSON, V. V., PRIVETTE, J. L., RIGGS, G., STRAHLER, A., LUCHT, W., MYNENI, R. B., KNYAZIKHIN, Y., RUNNING, S. W., NEMANI, R. R., WAN, Z., HUETE, A. R., VAN LEEUWEN, W., WOLFE, R. E., GIGLIO, L., MULLER, J.-P., LEWIS,

P., and BARNSLEY, M. J., 1998, The moderate resolution imaging spectroradiometer (MODIS): land remote sensing for global change research. *IEEE Transactions on Geoscience and Remote Sensing*, **36**, 1228–1249.

KAUFMAN, Y. J., JUSTICE, C. O., FLYNN, L. P., KENDALL, J. D., PRINS, E. M., GIGLIO, L., WARD, D. E., MENZEL, W. P., and SETZER, A. W., 1998, Potential global fire monitoring from EOS-MODIS. *Journal of Geophysical Research*, **103**, 32 215–32 238.

KUMMEROW, C., BARNES, W., KOZU, T., SHIUE, J., and SIMPSON, J., 1998, The tropical rainfall measuring mission (TRMM) sensor package. *Journal of Atmospheric and Oceanic Technology*, **15**, 808–816.

LYNNES, C., and MACK, R., 2001, An approach to data center-based KDD of remote sensing datasets. *Third Workshop on Mining Scientific Datasets, 7 April 2001, Chicago, II*.

MATSON, M., and DOZIER, J., 1981, Identification of subresolution high temperature sources using a thermal IR sensor. *Photogrammetric Engineering and Remote Sensing*, **47**, 1311–1318.

RIGGAN, P. J., BRASS, J. A., and LOCKWOOD, R. N., 1993, Assessing fire emissions from tropical savanna and forests of central Brazil. *Photogrammetric Engineering and Remote Sensing*, **59**, 1009–1015.

RITTER, N., 1994, MISR DID (DTED Intermediate Dataset) Subroutine Library Programmer's Guide. Jet Propulsion Laboratory, Pasadena, CA.

SIMKIN, T., and SIEBERT, L., 1994, *Volcanoes of the World: A Regional Directory, Gazetteer, and Chronology of Volcanism During the Last 10,000 Years* (Tucson, AZ: Geoscience Press).

STROPPIANA, D., PINNOCK, S., and GRÉGOIRE, J.-M., 2000, The Global Fire Product: daily fire occurrence from April 1992 to December 1993 derived from NOAA AVHRR data. *International Journal of Remote Sensing*, **21**, 1279–1288.